



Mixing of inelastic non-Newtonian fluids with inlet swirl

Dhananjay Kumar¹ and Pranab Kumar Mondal^{1,2,†}

¹Microfluidics and Microscale Transport Processes Laboratory, Department of Mechanical Engineering, Indian Institute of Technology Guwahati, Guwahati 781039, Assam, India

²School of Agro and Rural Technology, Indian Institute of Technology Guwahati, Guwahati 781039, India

(Received 10 October 2023; revised 1 May 2024; accepted 26 June 2024)

In the present work, the tangential (swirl) velocity component is superimposed at the intake of a narrow fluidic cylindrical pipe to achieve the desired mixing of inelastic non-Newtonian fluids/solutes at the outlet. We discuss an analytical method for obtaining the swirl velocity profile, considering the nonlinear viscous effects for both shear-thinning and shear-thickening fluids, represented by the power-law model. We numerically solve the species transport equation, coupled with the analytically derived swirl velocity, using our in-house developed code for the concentration distribution in the flow field. The results show that the inlet swirl and an increase in the shear-thinning fluid property improve advection-dominated mixing. Additionally, higher Reynolds numbers significantly enhance advection's dominance, as more rotation leads to the generation of vortices, resulting in an engulfment flow (chaotic convection) based mixing. We demonstrate that considering the increase in the shear-thinning fluid property with swirl intake reduces the amount of mixing time required in the convective regime.

Key words: laminar mixing, rheology, mixing enhancement

1. Introduction

The state-of-the-art development of microfluidic devices has gained attention from both academia and industry because of its widespread applications in biomedicine and biochemistry (Verpoorte & De Rooij 2003; Stone, Stroock & Ajdari 2004). It is worth mentioning that, unlike conventional procedures followed in the biochemical and biomedical industries, miniaturization techniques provide critical advantages such as reduced sample volumes, rapid processes, portability and a high surface-area-to-volume ratio (Djenidi & Moghtaderi 2006; Das *et al.* 2015). It is quite common for biofluids such as blood, synovial fluid, serum, saliva, nasal fluid, DNA solution, etc., which

† Email address for correspondence: pranabm@iitg.ac.in, mail2pranab@gmail.com

typically exhibit non-Newtonian behaviour, to experience laminar flow within such small fluidic channels. Notably, effective mixing, quick transportation, rapid testing and efficient diagnostics of samples/solutes with non-Newtonian fluid rheology are necessary for many biochemical processes and pathological diagnostics (Cosentino *et al.* 2015; Huang *et al.* 2016; Gaikwad, Mondal & Wongwises 2018; Herreman *et al.* 2021). As reported in the literature, researchers have employed both elastic and inelastic models to mimic the rheological and transport characteristics of such biofluids (Vagner & Patlazhan 2019; Nwani *et al.* 2022). It is important to add here that significant efforts have been made towards developing effective micromixers through geometrical modulation of flow configurations and the applications of external fields (Alekseenko *et al.* 1999; Krishnaveni *et al.* 2017; Mehta, Pati & Mondal 2021; Shyam, Mondal & Mehta 2021). In order to achieve proper mixing in on-chip microfluidic devices, simultaneously ensuring effective fluidic transport operations therein, researchers have developed numerous methodologies consistent with either passive methods or active techniques; all while articulating the underlying processes (Cetegen & Mohamad 1993; Djenidi & Moghtaderi 2006; Hadigol *et al.* 2011; Rezk *et al.* 2012; Chen *et al.* 2022).

To achieve effective and efficient advective mixing through passive methods, it is necessary to generate vortical flow in the mixing process (Afzal & Kim 2014; Matsunaga & Nishino 2014; Madana & Ashraf Ali 2020). However, such vortices tend to dissipate unless they are continuously sustained by the flow configuration/geometry. The dissipation of vortex or swirl has captivated researchers over the past century. Establishing swirl flow in the fluidic pathway requires implementation of a conducive flow configuration to instigate a swirling motion in the fluid. It may be mentioned here that a swirl flow environment can be developed through either a twisted tape set-up or by utilizing a swirl generator. In the much-celebrated experimental study by Taylor (1950), it was shown that the employment of a swirl generator at the inlet of the chosen fluidic pathway facilitates tangential fluid injection into the channel, which, in turn, leads to the generation of a primary vortex with a characteristic shape, known as the Rankine vortex (Reader-Harris 1994). Important to mention is that this swirling flow indicates the presence of a tangential velocity along the axial flow direction (Parchen & Steenbergen 1998).

Early works in this domain primarily focused on investigating the decay of swirl in pipes, both through theoretical and experimental approaches (Stokes *et al.* 2001a,b; Binagia *et al.* 2020). In the early 1950s, Talbot (1954) conducted theoretical and experimental studies on laminar swirling flows and revealed that the experimental swirl decay rates closely matched the theoretical predictions. Additionally, an unsteady theoretical flow analysis by Sibulkin (1962) was conducted for the vortex tube, and it was observed that the radial distributions of velocity and temperature at different axial locations qualitatively agreed with experimental results reported by Lay (1959). Subsequently, researchers examined the decay of swirl (Kreith & Sonju 1965; Steenbergen & Voskamp 1998) in fully developed turbulent flow environments through their analytical solution and identified the dependence of swirl velocity on Reynolds number (Re) and axial location. The decay in swirl, specified by swirl intensity, was found to follow an exponential trend, attributed to changes in parameters such as the wall friction factor, Reynolds number, transition radius and inlet swirl number (Morton 1969; Kitoh 1991; Yao & Fang 2012; Kumar, Shakya & Kaushik 2020; Kumar *et al.* 2023). Numerical simulations, as demonstrated by Kiya, Fukusako & Arif (1971), also assumed a Rankine vortex as the inlet swirl velocity profile. This assumption was based on experimental studies (Alekseenko *et al.* 1999) which showed that the swirl velocity in tubes is essentially a combination of the forced and free vortex components (Reader-Harris 1994). More recently, the decay of swirl intensity in

laminar flow of a non-Newtonian fluid was found to be influenced by the rheological nature of the fluid (Kathail, Pranav & Kaushik 2019).

However, recent developments in micro/mini fluidic applications within the medical industries have sparked a growing interest in the enhancement of transport and mixing of non-Newtonian fluids. We believe that harnessing the swirl velocity as a passive mixing technique for non-Newtonian fluids holds promise, particularly in laminar flow conditions. Therefore, in this current study, we aim to investigate the fundamental physics of decaying swirl and its influence on the mixing biofluids. Specifically, we seek to analyse how fluid rheology, imposed by vortical (swirl) flow within a narrow cylindrical tube, affects the complete mixing process between two similar inelastic non-Newtonian fluids. To achieve this, we first present an analytical solution for swirl velocity profiles and swirl decay, laying the groundwork for our investigation. Then, we utilize the analytical swirl velocity solution to numerically solve the species transport equation using an in-house finite volume-based code. With the results in hand, we discuss both the qualitative and quantitative aspects of mixing between two fluids in the context of decaying swirl flow in laminar regime.

2. Problem formulation and mathematical model

In this study, we execute a theoretical analysis to obtain the analytical expression for velocity fields of a non-Newtonian fluid, whose rheology is represented by the Ostwald–de-Waele power-law model. We consider the underlying flow through a narrow fluidic cylindrical pipe, driven by the inlet swirl (Taylor 1950). On using the analytically obtained velocity fields, we solve the species transport equation essentially for the concentration distribution in the chosen fluidic pathway.

2.1. Flow configuration: geometry and description

We consider the transport of non-Newtonian fluids through a cylindrical microfluidic pipe of radius R and length L , as shown in figure 1. The coordinate system describing the flow with coordinates r , θ and z , corresponding to velocity fields u_r , u_θ and u_z respectively, is attached to the inlet (left centre) of the channel. The inlet cross-sections of the entrances of fluids A and B are designated by $\theta = [0, \pi]$ and $[\pi, 2\pi]$, respectively. It may be mentioned here that the chosen configuration seems to mimic an application of blood flow getting infused with other biological species/reagents or the case of a DNA carrier fluid being mixed with the chemical reagents or fluorescent tracer particles (Cosentino *et al.* 2015). The concentrations of these fluids, such as blood or DNA carrier fluids, are identified by zero concentration ($C_0 = 0$), whereas the concentration of tracer particles or chemical reagents is identified by higher concentration ($C_0 = 1$) (see figure 1). The selection of such similar kinds of fluids also justifies the assumption of considering constant thermophysical properties, as well as non-Newtonian fluid behaviour in the underlying analysis.

Note that the fluids are considered to have same thermophysical properties and, therefore, one set of governing equations is solved for the flow field. Also, the characteristic length scale of the fluidic configurations, typical for a biomicrofluidic set-up, places the underlying flow in the fully developed laminar regime ($Re \sim 1$ to 100) (Matsunaga & Nishino 2014; Kaushik, Shyam & Mondal 2022).

2.2. Momentum transport: description of flow field

The governing equations (Deen 2016) describing the steady, incompressible and laminar flow of non-Newtonian fluid(s) through the chosen fluidic configuration, as shown schematically in figure 1, are the mass, momentum and species transport equations in

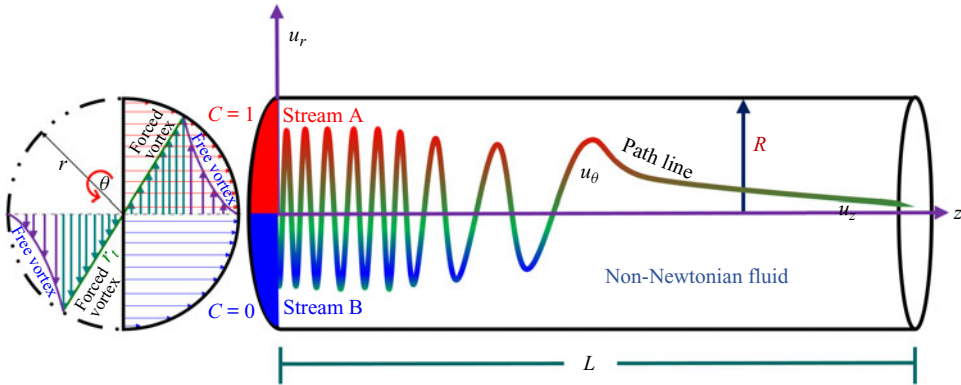


Figure 1. Schematic diagram describing the flow of non-Newtonian fluids with initial concentrations 1 and 0 in the upper and lower domains at the inlet of a pipe. A swirl motion consistent with the Rankine vortex is imposed at the pipe inlet. The coordinate system $(r - \theta - z)$ is attached at the centre of the pipe inlet.

a cylindrical coordinate system. It is worth mentioning here that we do not consider any body force in the present analysis. Below, we write the continuity and momentum transport equations for describing the underlying flow in the vectorial form

$$\nabla \cdot \mathbf{u} = 0, \tag{2.1}$$

$$\rho(\mathbf{u} \cdot \nabla)\mathbf{u} = -\nabla p + \nabla \cdot \boldsymbol{\tau}. \tag{2.2}$$

Note that, in the above (2.1)–(2.2), ρ is the fluid density, p is the fluid pressure, the velocity vector $\mathbf{u}(r, \theta, z) = u_r \mathbf{i}_r + u_\theta \mathbf{i}_\theta + u_z \mathbf{i}_z$ and $\nabla = (\partial/\partial r)\mathbf{i}_r + (\partial/r\partial\theta)\mathbf{i}_\theta + (\partial/\partial z)\mathbf{i}_z$.

The components of the deviatoric stress tensor ($\boldsymbol{\tau}$) in a cylindrical coordinate system for an incompressible power-law fluid are given as (Bird, Stewart & Lightfoot 2006; Deen 2016)

$$\left. \begin{aligned} \tau_{rr} &= \mu_e \left(2 \frac{\partial u_r}{\partial r} \right), & \tau_{\theta\theta} &= \mu_e \frac{2}{r} \left(\frac{\partial u_\theta}{\partial \theta} + u_r \right), \\ \tau_{zz} &= \mu_e \left(2 \frac{\partial u_z}{\partial z} \right), & \tau_{r\theta} = \tau_{\theta r} &= \mu_e \left(r \frac{\partial}{\partial r} \left(\frac{u_\theta}{r} \right) + \frac{1}{r} \frac{\partial u_r}{\partial \theta} \right), \\ \tau_{\theta z} = \tau_{z\theta} &= \mu_e \left(\frac{\partial u_\theta}{\partial z} + \frac{1}{r} \frac{\partial u_z}{\partial \theta} \right), & \tau_{zr} = \tau_{rz} &= \mu_e \left(\frac{\partial u_z}{\partial r} + \frac{\partial u_r}{\partial z} \right). \end{aligned} \right\} \tag{2.3}$$

Here, μ_e is the effective viscosity for the power-law fluid and it is given as $\mu_e = \mu_0(\sqrt{0.5(\mathbf{D} : \mathbf{D})})^{n-1}$, where μ_0 is the flow consistency index, n is the power-law index and \mathbf{D} stands for the deformation tensor defined as $\mathbf{D} := \nabla \mathbf{u} + (\nabla \mathbf{u})^T$.

To solve (2.1)–(2.2) analytically, we consider that the flow is axisymmetric with negligible body force and becomes fully developed along the axial direction i.e. $u_z = u_z(r)$ (Kumar *et al.* 2020). Considering the aforementioned assumptions, the component of the flow velocity in the radial direction is calculated to be constant using the continuity (2.1) and proven to be zero ($u_r = 0$), consistent with the no-slip condition at the wall. Proceeding further with this condition and using (2.3), the momentum transport equation in the radial direction reduces to $\rho(u_\theta^2/r) = \partial p/\partial r$, yielding the relation between the radial pressure gradient and the tangential velocity component. It shows that the radial variation of pressure simply supplies the force necessary to keep the fluid elements moving through a circular path within the channel.

Consequently, to solve the momentum transport equation (2.2), the physically justified boundary conditions, based on the aforementioned discussion and assumptions, in compact form are given as: $u_r = 0$; $\partial u_z / \partial r|_{r=0} = 0$, $u_z(r)|_{r=R} = 0$; $u_\theta(r, z)|_{r=0} = 0$, $u_\theta(r, z)|_{r=R} = 0$. At the inlet ($z=0$) of the considered fluidic configuration, a Rankine vortex (Yao & Fang 2012; Kumar *et al.* 2020) is imposed to create the swirl, i.e. $u_\theta(r, z)|_{z=0} = \{(u_{\theta,i,max})(r/r_t), r \leq r_t$ and $(u_{\theta,i,max})(r_t(R - r)/r(R - r_t))\}$, $r \geq r_t$. Here, $u_{\theta,i,max}$ and r_t represent the maximum inlet swirl velocity and transition radius, respectively. The dimensional transition radius, denoted as r_t , signifies the point where the transition from a forced to a free vortex occurs at the channel inlet. Now, in order to solve the flow velocity component in the azimuthal direction, first, we solve the axial momentum, which will then be superimposed to find the tangential velocity component.

2.2.1. Analytical solution

We write the reduced form of the momentum transport equation (2.2) in the axial direction as follows:

$$0 = -\frac{\partial p}{\partial z} + \left[\frac{1}{r} \frac{\partial}{\partial r} (r\tau_{rz}) \right] = -\frac{\partial p}{\partial z} + \left[\frac{1}{r} \frac{\partial}{\partial r} \left(r\mu_e \left(\frac{\partial u_z}{\partial r} \right) \right) \right]. \tag{2.4}$$

To obtain (2.4), we refer to the components of the deviatoric stress tensor through (2.3) and use axisymmetric ($\partial/\partial\theta = 0$) as well as fully developed flow ($u_z = u_z(r)$) assumptions.

In addition, with the order of magnitude analysis, the effective viscosity is derived as $\mu_e = \mu_0 |\partial u_z / \partial r|^{n-1}$ (Sarma, Gaikwad & Mondal 2017). Substituting the value of μ_e and employing the boundary conditions, i.e. $\partial u_z / \partial r|_{r=0} = 0$ and $u_z(r/R = 1) = 0$, respectively, we solve (2.4) for the expression of axial velocity, which reads as

$$\begin{aligned} u_z &= \left(\frac{n}{n+1} \right) \left(\frac{R^{n+1} |\Delta p|}{2\mu_0 L} \right)^{1/n} \left[1 - \left(\frac{r}{R} \right)^{(n+1)/n} \right] \\ &= \left(\frac{3n+1}{n+1} \right) u_{av} \left[1 - \left(\frac{r}{R} \right)^{(n+1)/n} \right]. \end{aligned} \tag{2.5}$$

In (2.5), $u_{av} = \int u_z dA / \int dA = (n/(3n+1))((R^{n+1} |\Delta p|)/(2\mu_0 L))^{1/n}$ represents the average axial flow velocity.

We write the simplified form of (2.2) using the aforementioned assumptions to obtain the tangential momentum equation as follows:

$$\begin{aligned} u_z \frac{\partial u_\theta}{\partial z} &= \frac{1}{\rho} \left[\frac{1}{r^2} \frac{\partial}{\partial r} (r^2 \tau_{r\theta}) + \frac{\partial}{\partial z} (\tau_{\theta z}) \right] \\ &= \frac{1}{\rho} \left[\frac{1}{r^2} \frac{\partial}{\partial r} \left(r^2 \mu_e \left(r \frac{\partial}{\partial r} \left(\frac{u_\theta}{r} \right) \right) \right) + \frac{\partial}{\partial z} \left(\mu_e \left(\frac{\partial u_\theta}{\partial z} \right) \right) \right]. \end{aligned} \tag{2.6}$$

Employing the assumptions discussed before and using the deviatoric stress components as delineated in (2.3), we make an effort to write (2.6) in the reduced form. Note that (2.6) is the reduced form of the tangential momentum equation and is obtained by employing a few assumptions, i.e. axisymmetric flow ($\partial/\partial\theta = 0$) and fully developed flow ($u_z = u_z(r)$) together with the consideration of the continuity equation ($u_r = 0$), as discussed in § 2.2. As is apparent from (2.6), we have discarded the axial diffusion term i.e. $\partial^2 u_\theta / \partial z^2$. We perform an order of magnitude analysis to justify the omission of the axial diffusion term from (2.6) as follows. In this analysis, we have imposed swirl motion on the constituent

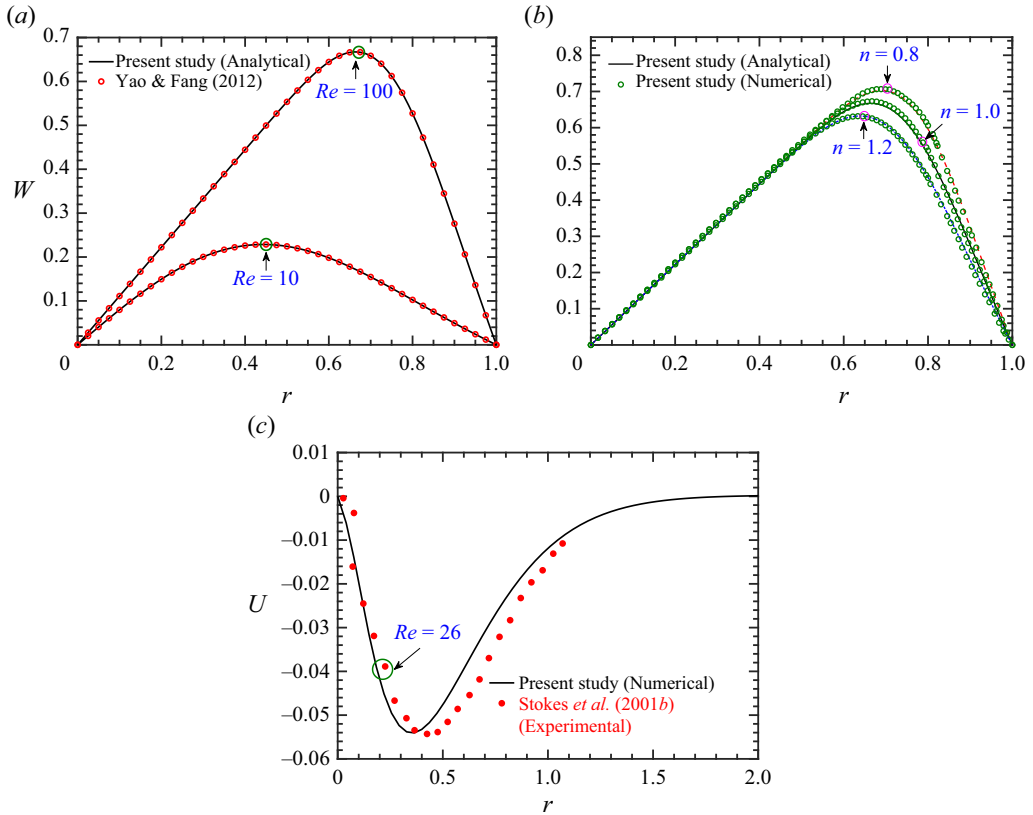


Figure 2. Validation of present analytical swirl velocity profile (a) with Yao & Fang (2012) at $Re = 10$ and 100 for Newtonian fluid ($n = 1.0$) and (b) with the three-dimensional numerical simulation (ANSYS) results for non-Newtonian fluid at power-law index, $n = 0.8, 1.0, 1.2$. The other parameters considered for validation are $Re = 100$, axial location, $z = 1$ and transition radius, $r_t = 0.9$. Panel (c) represents the validation of existing experimental results of the axial velocity profile and present numerical model at $Re = 26$ with limiting case for a Newtonian fluid, $n = 1$.

fluids at the inlet to obtain enhanced mixing. Now, even in the presence of an imposed swirl motion, we see that the magnitude of the tangential velocity (u_θ) is less than the axial velocity (u_z) even in the regime very close to the pipe inlet (here, $u_{\theta,max}/u_{avg}|_{Re=10,100} \sim 0.2, 0.7$; $u_{z,max}/u_{avg} = 2$; cf. figure 2a). Certainly, at further downstream locations of the pipe, the tangential velocity will be even smaller because of the swirl decay compared with the fully developed axial flow velocity. Important to mention is that we have considered $L = 120R$ in this analysis, signifying that $R \ll L$. Thus, a relatively smaller magnitude of tangential velocity together with larger axial length allow us to discard the axial diffusion term, which is $\partial^2 u_\theta / \partial z^2 \sim u_\theta / L^2 \ll 1$. As such, the magnitude of the axial diffusion term is an order less than the diffusion in the radial direction. Consistent with this order of magnitude analysis, we have discarded the axial diffusion term in (2.6). Substituting the effective viscosity $\mu_e = \mu_0 |\partial u_z / \partial r|^{n-1}$ (Sarma *et al.* 2017) in (2.6), we obtain the dimensionless form of (2.6) in the following form:

$$K_0 U r^2 \frac{\partial W}{\partial Z} = \left[\frac{\partial}{\partial r} (r^{(3n-1)/n}) \left(\frac{\partial W}{\partial r} - \frac{W}{r} \right) \right]. \quad (2.7)$$

In (2.7), the term $K_0 = Re(-1)^{n-1}(n/(3n + 1))^{n-1}$, where the Reynolds number, $Re = \rho u_{av}^{2-n} R^n / \mu_0$. Here, K_0 is analysed under the consideration of real values while varying the power-law index, n . The dimensionless variables appearing in (2.7) are $U(r) = u_z / u_{av}$; $W(z, r) = u_\theta / u_{av}$; $r \sim r^* = r/R$; $z \sim z^* = z/R$, $r_t \sim r_t^* = r_t/R$; where r_t^* represents the non-dimensional transition radius between a forced and a free vortex. It is worth mentioning here that the chosen scales (velocity and length) in this endeavour are consistent with those used in the seminal works reported in the literature (Kreith & Sonju 1965; Ingham *et al.* 1990; Tumin 1996; Rouquier, Poth erat & Pringle 2019; Kim 2024).

To solve (2.7), which is a nonlinear partial differential equation, we apply axisymmetric and no-slip boundary conditions with $W(z, r = 0) = 0$ and $W(z, r = 1) = 0$, respectively. Note that a Rankine vortex is imposed at the inlet ($z = 0$) to create the swirl motion therein. The dimensionless form of the Rankine vortex (Yao & Fang 2012; Kumar *et al.* 2020) is given by

$$W(z = 0, r) = \begin{cases} \frac{u_{\theta,i,max}}{u_{av}} \frac{r}{r_t}, & r \leq r_t \text{ and} \\ \frac{u_{\theta,i,max}}{u_{av}} \frac{r_t(1 - r)}{r(1 - r_t)}, & r \geq r_t. \end{cases} \quad (2.8)$$

In this endeavour, we look for the analytical solution of the tangential velocity component. Employing a technique consistent with the separation of variables method and defining $W(z, r) = F(z)G(r)$, we solve the nonlinear partial differential equation (2.7) by reducing it to two ordinary differential equations (ODEs) essentially to obtain the tangential velocity component. Below, we write the ODEs with the consideration of λ as positive constant

$$K_0 \frac{dF}{dz} + \lambda^2 F = 0, \quad (2.9)$$

$$(r^{(3n-1)/n}) \frac{d^2G}{dr^2} + (2n - 1/n) \frac{dG}{dr} + (\lambda^2 U r^2 - (2n - 1/n) r^{n-1}) G = 0. \quad (2.10)$$

Further, to obtain the analytical series solution, we consider λ as constant positive real eigenvalue and make use of the axisymmetric boundary condition (i.e. $W(z, 0) = 0$). We obtain the swirl flow velocity $W(z, r)$ in terms of eigenvalues (λ_m ; where $m = 1, 2, \dots \infty$) and by using symbolic notation for function WhittakerM as

$$\text{WhitM}_{m,n} = \text{WhittakerM} \left[\frac{n\lambda_m \sqrt{3n + 1}}{(2(n + 1)^{3/2})}, \frac{3n - 1}{(2n + 2)}, \frac{(2n\lambda_m) r^{((n+1)/n)} \sqrt{3n + 1}}{(n + 1)^{3/2}} \right]. \quad (2.11)$$

The swirl velocity is obtained by combining the solutions of the aforementioned ODEs (2.9) and (2.10). Below, we present the swirl velocity profile by utilizing the above notation for the Whittaker function (WhittakerM) as ‘WhitM_{m,n}’ as follows:

$$W(z, r) = \sum_{m=1}^{\infty} C_m \exp(-\lambda_m^2 z / K_0) (\text{WhitM}_{m,n} / r). \quad (2.12)$$

Here, WhittakerM(a, b, r) is the special function for the solution of Whittaker’s equation. Note that WhittakerM(a, b, r) is the modified form of the confluent hypergeometric equation and it is defined as (Whittaker 1903; Abramowitz & Stegun 1970) WhittakerM(a, b, r) = $(\exp(-0.5r))(r^{b+0.5})M(b - a + 0.5, 1 + 2b, r)$,

where $M(a, b, r) = \sum_{k=0}^{\infty} (a^k)(k)/(b^k)(k!)$ is Kummer's confluent hypergeometric function.

Substituting the value of the power-law index $n = 1$, representing a special case of a Newtonian fluid, the solution can be written as

$$W(z, r) = \sum_{m=1}^{\infty} C_m \exp(-\lambda_m^2 z/Re) \left(\text{WhittakerM} \left[\frac{\lambda_m}{2\sqrt{2}}, \frac{1}{2}, \sqrt{2}\lambda_m r^2 \right] \right) / r. \tag{2.13}$$

We consider the first 30 eigenvalues of (2.12), obtained using the no-slip boundary condition, i.e. $W(z, r = 1) = 0$, to get a convergence of the order 10^{-12} for different values of the power-law index ($n = 0.8, 1.0, 1.2$). Employing this specified boundary condition, i.e. $W(z, r = 1) = 0$

$$\sum_{m=1}^{\infty} \text{WhittakerM} \left[\frac{n\lambda_m\sqrt{3n+1}}{(2(n+1)^{3/2})}, \frac{3n-1}{(2n+2)}, \frac{(2n\lambda_m)\sqrt{3n+1}}{(n+1)^{3/2}} \right] = 0. \tag{2.14}$$

We derived the above expression to obtain the eigenvalues. We consider a numerical method, consistent with the iterative approach, to determine the eigenvalues of the function

$$f = \sum_{m=1}^{\infty} \text{WhittakerM} \left[\frac{n\lambda_m\sqrt{3n+1}}{(2(n+1)^{3/2})}, \frac{3n-1}{(2n+2)}, \frac{(2n\lambda_m)\sqrt{3n+1}}{(n+1)^{3/2}} \right] = 0. \tag{2.15}$$

The method is applied for different values of n , assuming that f is a continuous function. The characteristic function f is considered to possess m real roots, as denoted by $\lambda_1, \lambda_2, \dots$ and λ_m . The roots of the real-valued function $f = 0$ are determined using the bisection method (Henderson & Aldridge 1992; Grassia 2020). In this method, the interval limits $[a, b]$ for first iteration are initially set to the lower bound $a = 1$ and upper bound $b = 4$. The subsequent finite eigenvalues (λ_i , where $i = 1, 2, \dots, 30$) are calculated by ensuring that the condition $(f(a) \times f(b)) < 0$ is satisfied, indicating that the roots are located within the specified interval. Here, the bisection method is chosen for its simplicity, reliability and effectiveness in finding isolated single roots in a fixed range. In table 1, we present only the first ten (10) eigenvalues for different values of the power-law index ($n = 0.8, 1.2$), including $n = 1.0$ (Newtonian fluid). It may be added here that we undertake an effort to cross-verify our solution methodology, and in doing so, we compare the calculated eigenvalues for $n = 1$ with the reported results of Yao & Fang (2012), included in table 1 as well. Important to mention is that the calculated eigenvalues for $n = 1.0$ conform to those reported by Yao & Fang (2012). We, however, will make all 30 eigenvalues available to the readers upon request. By appealing to Sturm–Liouville theorem (Kaplan 1981), we calculate the value of C_m , a coefficient appearing in (2.12), by applying the orthogonality condition of the eigenfunctions. We establish orthogonality conditions by considering distinct eigenvalues, denoted as λ_m and λ_{m1} . Specifically, when $\lambda_m \neq \lambda_{m1}$, we rely on the Sturm–Liouville theorem (Kaplan 1981), employing a weight function defined as $r(1 - r^{((n+1)/n)})$, within the interval $[0,1]$. This weight function ensures orthogonality of the eigenfunctions. The orthogonality condition is expressed as follows:

$$\int_{r=0}^{r=1} \frac{\text{WhittakerM} \left[\frac{n\lambda_m\sqrt{3n+1}}{(2(n+1)^{3/2})}, \frac{3n-1}{(2n+2)}, \frac{(2n\lambda_m)r^{((n+1)/n)}\sqrt{3n+1}}{(n+1)^{3/2}} \right]}{r}$$

m	$n = 0.8, \lambda_m$	$n = 1.0, \lambda_m$	$n = 1.2, \lambda_m$
1	3.43962	3.26973	3.14988
2	6.72326	6.11470	5.70642
3	10.00036	8.94845	8.24912
4	13.27591	11.77938	10.78820
5	16.55087	14.60923	13.32586
6	19.82557	17.43855	15.86282
7	23.10011	20.26760	18.39940
8	26.37457	23.09647	20.93575
9	29.64897	25.92523	23.47194
10	32.92333	28.75392	26.00804

Table 1. The first ten eigenvalues for the generalized Whittaker function having values of power-law index, $n = 0.8, 1.0$ and 1.2 .

$$\begin{aligned} & \text{WhittakerM} \left[\frac{n\lambda_{m1}\sqrt{3n+1}}{(2(n+1)^{3/2})}, \frac{3n-1}{(2n+2)}, \frac{(2n\lambda_{m1})r^{((n+1)/n)}\sqrt{3n+1}}{(n+1)^{3/2}} \right] \\ & \times \frac{1}{r} \\ & \times r(1 - r^{((n+1)/n)}) dr = 0. \end{aligned} \tag{2.16}$$

Utilizing the Sturm–Liouville theorem and the orthogonality of eigenfunctions at $\lambda_m = \lambda_{m1}$, with the inlet condition (2.8), the coefficient C_m mentioned in (2.12) can be obtained as

$$\begin{aligned} C_m = & \int_{r=0}^{r=1} W(0, r) \left(\frac{(\text{WhitM}_{m,n})}{r} \right) r(1 - r^{((n+1)/n)}) dr / \\ & \left(\int_{r=0}^{r=1} \left[\frac{(\text{WhitM}_{m,n})}{r} \right]^2 r(1 - r^{((n+1)/n)}) dr \right). \end{aligned} \tag{2.17}$$

In order to quantify the intensity of swirl along the channel, we define below in (2.18) a dimensionless swirl number $S(z)$ as the ratio of the axial flux of angular momentum to the axial flux of axial momentum at a particular cross-section (Reader-Harris 1994; Alekseenko *et al.* 1999; Maddahian *et al.* 2011)

$$S(z) = \int_0^R u_z^* u_{\theta}^{*2} r^{*2} dr^* / \left(R \int_0^R u_z^{*2} r^* dr^* \right) = \int_{r=0}^{r=1} UW r^2 dr / \left(\int_{r=0}^{r=1} U^2 r dr \right). \tag{2.18}$$

Using (2.8) and (2.12) in (2.18), the ratio $S(z)/S(0)$, i.e. the ratio of the swirl number $S(z)$ at any axial location to the that at the inlet, can be obtained as

$$\frac{S(z)}{S(0)} = \frac{\sum_{m=1}^{\infty} C_m \exp(-\lambda_{m1}^2 z / K_0) \int_{r=0}^{r=1} (\text{WhitM}_{m,n}) r(1 - r^{((n+1)/n)}) dr}{\int_{r=0}^{r=1} W(0, r) r^2 (1 - r^{((n+1)/n)}) dr}. \tag{2.19}$$

Having established the analytical expression of both the axial and tangential velocity profiles, we quantify mixing of two fluids/solutes as elaborated in the next sub-section.

For this part, we first obtain the spatial distribution of the species concentration in the chosen fluidic pathway and then calculate the underlying mixing efficiency for different values of the power-law index.

2.2.2. Benchmarking of analytical method and selection of parameters

To substantiate the efficacy of the proposed theoretical framework, we consider the triple benchmarking strategy as graphically presented in figure 2(a–c). In figure 2(a), we plot the swirl velocity profile obtained from the present theoretical framework in the limiting case of a Newtonian fluid, i.e. $n = 1$, for two different values of Re ($= 10, 100$) and compare the same with the reported profile of Yao & Fang (2012). The other parameters considered for this plot are $z = 1, r_t = 0.9$. It is noteworthy that, to obtain the analytical solution of the swirl velocity using (2.10), the values of λ_m , crucial in satisfying the no-slip boundary condition i.e. $W(z, r = 1) = 0$, are independent of the Reynolds number – a point emphasized by Kumar *et al.* (2020) and Yao & Fang (2012). It may be mentioned here that analytical solutions for both no-slip and slip cases have been established in the literature as well (Kumar *et al.* 2020). To verify the convergence of our results, we performed a validation analysis in figure 2(a) by comparing the eigenvalues obtained from our calculation with those reported by Yao & Fang (2012) for $Re = 10$ and 100. This benchmarking endeavour ensures the accuracy and consistency of our results. A closer match between the present and published results, as witnessed in figure 2(a), vouches for the efficacy of the proposed analytical model.

Effort has been taken in figure 2(b) to compare our analytical solutions of the flow velocity for different non-Newtonian fluids, including both shear-thinning ($n = 0.8$) and shear-thickening ($n = 1.2$) fluids with the corresponding full-scale simulated results. For this validation, we performed three-dimensional simulations employing the finite volume framework of ANSYS Fluent and considered an identical flow configuration as chosen in this endeavour. For the plots depicted in figure 2(b), the other parameters are $z = 1, r_t = 0.9$ at $Re = 100$. To ascertain the credibility of the theoretical framework developed in our analysis, or more precisely, to ascertain the correctness of the analytical solutions, obtained considering a few assumptions, we performed another validation to compare the analytically obtained flow velocity for non-Newtonian fluids (shear-thinning and shear-thickening fluids) with the full-scale simulated results. We wish to emphasize that the finite volume method framework of ANSYS Fluent is employed in this study to obtain simulated results and subsequently to validate them with the analytical results as presented in figure 2(b). We used the Semi-Implicit Method for Pressure-Linked Equations (SIMPLE) algorithm of the ANSYS Fluent solver for pressure–velocity coupling and employed a second-order upwind scheme to discretize the momentum transport equations (Patankar 1980). We obtain a closer match between analytical swirl velocity profiles and the corresponding numerical results for three different values of n of 0.8, 1.0 and 1.2, as shown in figure 2(b). The comparison analysis presented in figure 2(b) underscores that our analytical solutions, obtained by considering a few physically justified assumptions, faithfully capture the full-scale (three-dimensional) simulated results. It is imperative to note that the validation of the analytical results through a comparison with full-scale numerical simulations using ANSYS Fluent underlines the credibility of the proposed analytical framework. For the sake of completeness, we mention here that the simulations were performed considering a total 12081477 control volumes and assigning a residual criterion of 10^{-7} for all the transport variables. As evident from figure 2(b), analytical calculations obtained for all the values of n ($= 0.8, 1.0, 1.2$) match in a fairly accurate

manner with the simulated results. Furthermore, we undertake an effort in [figure 2\(c\)](#) to compare the simulated axial velocity profile with the experimental results available in this paradigm (Stokes *et al.* 2001*b*). It is worth mentioning here that the experimental validation is limited to a Newtonian fluid ($n=1.0$), while the parameters considered are as follows: $Re=26$ and $r_t=0.5$. Consistent with the experimental configuration as considered by the authors in their study (Stokes *et al.* 2001*b*), we consider only the Rankine vortex with an angular velocity of 13.04 rad s^{-1} at the inlet. Important to mention is that the swirl specified at the inlet has two different configurations over the domain as follows: force vortex structure up to transition radius and free vortex regime afterwards. Depicted variations in [figure 2\(c\)](#) vouch for a closer as well as consistent match between the experimental and full-scale simulated results without considering the axisymmetric and fully developed flow.

We observe that, for the considered values of Re , our analytical framework developed to solve for the swirl momentum transport can predict the swirl velocity profile reported by Yao & Fang (2012). Quite notably, the present analytical solutions closely match with full-scale three-dimensional simulated results as well. Notably, this model benchmarking endeavour justifies the accurateness of our modelling framework, which in turn, ascertains the credibility of the analytical solutions as well. As endorsed by the benchmarking analyses, as presented above, we consider the analytically derived velocity profile to obtain the concentration field in the fluidic pathway essentially to save computational time and effort.

For the present analysis, we consider the ranges of $Re \sim 1-10^2$ and $n \sim 0.6-1.4$ (Matsunaga & Nishino 2014; Cortes-Quiroz, Azarbadegan Zangeneh 2017; Majhi, Nayak & Weigand 2023). It may be mentioned here that, to analyse the mixing performance in this endeavour, we vary the transition radius ratio from 0.7 to 0.9 by keeping the Péclet number, $Pe (= 2600)$ constant (Rezk *et al.* 2012).

2.2.3. Description of flow field

Researchers have concluded that the generation of a vortex leads to the chaotic nature between fluid layers and helps to attain efficient mixing of two fluids/solutes in a shorter length. To understand the vortex-assisted mixing of non-Newtonian fluids in a narrow fluidic channel, which is the prime focus of this endeavour, we develop a mathematical model. Our modelling framework employs a semi-analytical technique for solving the momentum transport equation, coupled with the finite volume-based numerical method for the species transport equation, as discussed in § 2.2. In the present analysis, we focus on the rate of change of Rankine vortex strength and its influence on the underlying mixing of two constituent non-Newtonian fluids, investigated for a window of pertinent parameters such as Reynolds number, power-law index and transition radius. We consider an inlet swirl number equal to one throughout this investigation in order to avoid disparaging statements regarding the supremacy of angular momentum and axial momentum in the field. We begin with the description of the swirl velocity profile as demonstrated in [figure 2\(a,b\)](#). As seen in [figure 2\(a,b\)](#), the swirl velocity profile starts to decrease in the outer region along the outward radial direction after it reaches its maximum value.

[Figure 3](#) shows the variation of the swirl velocity and swirl decay profile with a change in the power-law index. For fluids with higher n values, as shown in [figure 3](#), more time is needed for the viscous force to impede the swirl velocity. The magnitude of peak swirl velocity decreases more strongly for fluids with increasing n due to the stronger viscous effect (caused by larger effective viscosity), as shown in [figure 3\(a\)](#). Also, the variation of the swirl velocity profile for different values of transition radius ($r_t = 0.7, 0.9$), obtained

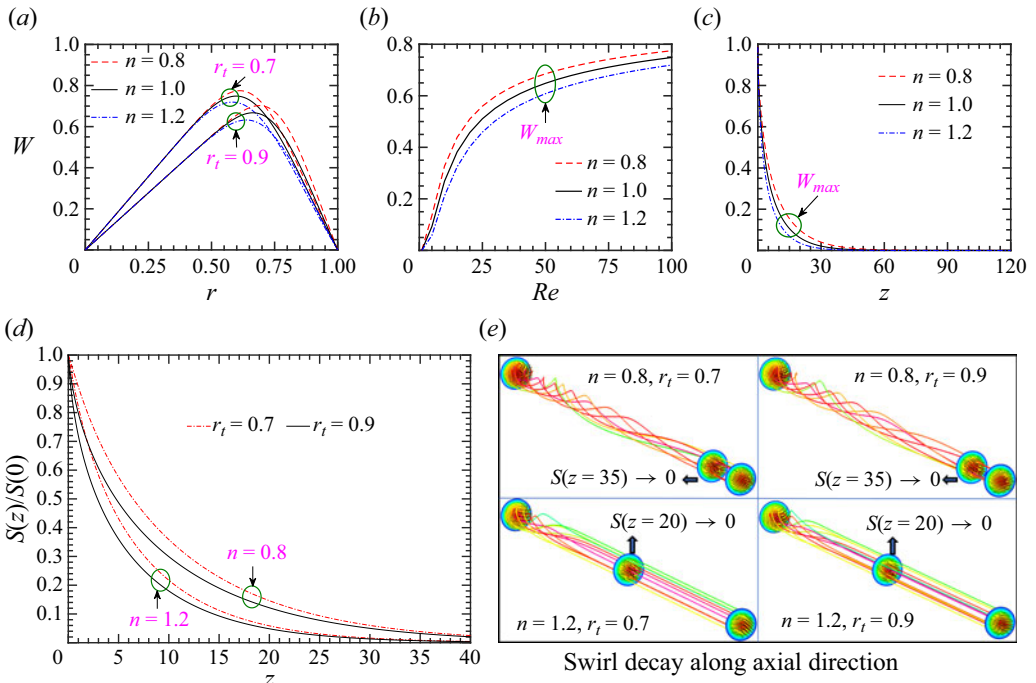


Figure 3. Plot showing the analytical swirl velocity profiles for different values of power-law index $n = 0.8, 1.0, 1.2$ and at an axial location $z = 1$. (a) Variation with pipe radius for two different values of transition radii (r_t) of 0.7 and 0.9. (b) Variation of maximum swirl velocity with Reynolds number (1 to 100) with transition radius $r_t = 0.7$. (c) Axial variation of maximum swirl velocity for $Re = 100, r_t = 0.7$. (d) Plots depicting the axial variation of swirl intensity for $n = 0.8$ and 1.2, considering other parameters as $r_t = 0.7, 0.9$ and $Re = 100$. (e) Qualitative prediction of swirl velocity decay, as shown by the path lines obtained from numerical (ANSYS Fluent) solutions at axial planes ($z = 20$ and 35) for $n = 0.8$ and 1.2, while the other parameters considered are $Re = 100, r_t = 0.7$ and 0.9.

at $Re = 100, z = 1$, is shown in figure 3(a). For the shear-thickening fluids with larger n value, a relatively higher effective viscosity promotes the transmission of the zero momentum at the wall deeper into the pipe, as witnessed by the offset of the point of the peak velocity radially inward towards the axis of the channel. This phenomenon further lowers the magnitude of the swirl velocity peak, as confirmed in figure 3(a). Figure 3(a) illustrates how the swirl velocity profile deviates significantly for larger values of r_t with the change in power-law index close to the inlet of the channel ($z = 1$). This is directly caused by the fact that the higher velocity gradients lead to an increase in the effective viscosity of a shear-thickening fluid. Additionally, given the Rankine vortex is imposed at the inlet, which is evident from the presence of a radial pressure gradient from core to annuls, the transition occurs at $r = r_t$ is a function of swirl velocity and radius of the channel. The formation of boundary layer ensures that there is a velocity gradient in the flow field. It may be added here that the shear effect predominates closer to the wall and gradually diminishes along the radial direction towards the axis of the channel, which affects the free vortex flow. Although there is a smooth transition from a forced to a free vortex, it is established that, closer to the inlet, the peak value always occurs at radii less than the transition radius. This is due to the frictional effects of the wall on the free vortex

region. With decreasing transition radius, the magnitude of the swirl velocity increases in order to retain the momentum in the radial direction for a fixed value of Re .

Figure 3(b) plots the variation of swirl velocity versus Re in the range $1 \leq Re \leq 100$. As seen from figure 3(b), the magnitude of the swirl velocity increases substantially on increasing the value of Re , while for a given Re , the swirl velocity becomes higher for shear-thinning fluids. The primary flow parameter that plays crucial role in swirl-driven flows is the Re , typically calculated based on the average axial velocity. The higher Re accelerates the swirl's motion into the channel. Consequently, as shown in figure 3(b), the maximum magnitude of the swirl velocity, represented by W_{max} , increases with an increase in Re from 1 to 100 for $r_t = 0.7$, calculated at an axial location $z = 1$. The highest magnitude of swirl tends to remain in its radial location following the interaction between swirl modulated advective effects and fluid viscous effects. As a result, the influence of the channel surface on the wall viscosity causes the swirl velocity to travel as closely as possible along the pipe axis. Also, a more viscous nature of the constituent fluids, as realized by an increasing the shear-thickening effect, results in a reduction of W_{max} with an increase in Re .

We show, in figure 3(c), the decay of the maximum swirl velocity (W_{max}) along the axial direction for three different values of n ($= 0.8, 1.0$ and 1.2), the other parameters being $Re = 100$ and $r_t = 0.7$. The decay of W_{max} is slower for the shear-thinning fluids compared with the shear-thickening fluids. It is important to observe from figure 3(c) that, for the shear-thinning fluids, the swirl velocity travels much deeper into the channel inside before dissipation. This happens due to the larger velocity gradient near the channel wall that tends to increase the shear stress therein for shear-thickening fluids, which in turn, accelerates the swirl velocity decay compared with shear-thinning fluids.

Figure 3(d) demonstrates the intensity of swirl decay along the axial direction for both the shear-thinning ($n = 0.8$) and shear-thickening, ($n = 1.2$) fluids. The plots are depicted for two different values of transition radii $r_t = 0.7, 0.9$ and obtained at $Re = 100$. It is apparent from the description made in the preceding section(s) that, for a given value of Re , the magnitude of the swirl becomes higher and at smaller transition radius. This finding is consistent with the observation we established in our earlier discussion pertaining to the relationship between the swirl velocity and Reynolds number. This can be explained by the fact that, as the transition radius increases, the swirl velocity gradient increases close to the channel wall. A larger velocity gradient near the channel wall tends to increase the shear stress therein and speed up the swirl velocity's decay. Furthermore, irrespective of the magnitude of Re , the increased viscous effect at higher transition radii tends to speed up the swirl decay for higher values of the power-law index. As can be seen from figure 3(d), the effect of the transition radius is more prominent on the swirl momentum transport of shear-thinning fluids ($n < 1$) compared with shear-thickening fluids ($n > 1$). Also, figure 3(d) witnesses that the swirl velocity decay is somewhat higher for larger transition radii. We attribute this observation to the increased shear stress developed at higher transition radii owing to the larger velocity gradients. It can be inferred from the foregoing discussion as follows: fluids that thin out under shear would have an enhanced transport capability at smaller transition radii than fluids that thicken under shear. Shear-thickening (dilatant) fluids should not be used in applications that demand an extended swirl effect since this special class of fluids promotes swirl to decay more quickly than shear-thinning (pseudoplastic) fluids.

In figure 3(e), we show a qualitative description of swirl transport and its decay for different fluids to facilitate a better understanding of the results at hand. The other parameters considered for this plot are $Re = 100$, $r_t = 0.7$ and 0.9 . The streamlines

emerging from the channel entry are portrayed in figure 3(e) to provide greater insights into the swirl decay. Note that the plots depicted are obtained from simulations. Figure 3(e) witnesses (see supplementary movies 1–4 available at <https://doi.org/10.1017/jfm.2024.792> for a clear insight) that swirl decay occurs nearly at an axial location $z=35$ and 20 for shear-thinning fluids ($n=0.8$) and shear-thickening fluids ($n=1.2$), respectively, from the inlet of the chosen fluidic configuration. We would like to discuss two important aspects, as observed from figure 3(e). First, for the shear-thinning fluids ($n=0.8$), the swirl momentum penetrates a greater distance along the channel length for a given strength of inlet swirl, Re ($= 100$) and r_i . This observation on complying with our earlier explanation signifies the impact of rheology modulated fluid viscosity on the swirl transport. Second, the inlet swirl induces an azimuthal motion within the fluid layers, enhancing the contact area and chaotic interaction between the participating fluids. This enhancement in convective-based mixing is particularly significant irrespective of the fluid rheology, emphasizing the enduring impact of the inlet swirl in promoting efficient mixing within the system. This qualitative representation of swirl transport in figure 3(e), derived from full-scale simulations, harmonizes closely with the quantitative analysis of swirl decay presented in figure 3(d). The coherence observed between our analytical solutions and full-scale simulated results once more underlines the credibility of the analytical technique proposed in this analysis.

2.3. Species transport: description of concentration field

Consistent with the assumptions considered in this analysis, except for the axisymmetric one (as the constituent two fluids occupy either half of the pipe inlet cross-section), the simplified species transport equation for zero radial flow velocity can be written in the form as given below

$$u_\theta \frac{1}{r} \frac{\partial C^*}{\partial \theta} + u_z \frac{\partial C^*}{\partial z} = D_0 \left[\frac{1}{r} \frac{\partial}{\partial r} \left(r \frac{\partial C^*}{\partial r} \right) + \frac{1}{r^2} \frac{\partial^2 C^*}{\partial \theta^2} + \frac{\partial^2 C^*}{\partial z^2} \right]. \quad (2.20)$$

Here, C^* is solute concentration and D_0 is the diffusion coefficient of non-Newtonian fluids. To distinguish the species concentration of constituent fluids/solutes in the flow domain, we assign $C^* = 1$ for stream A (red colour) and $C^* = 0$ for stream B (blue colour), as shown in figure 1.

To non-dimensionalize equation (2.20), we use the velocity and length scales already defined in § 2.2.1, while we define dimensionless concentration $C = C^*/C_0$. Here, C_0 is the initial concentration of stream A. It is worth mentioning here that, considering a few factors, typically used by the researchers in this paradigm (Matsunaga & Nishino 2014; Cortes-Quiroz *et al.* 2017; Majhi *et al.* 2023), we select the aforementioned initial species concentration of the candidate fluids. For the sake of the completeness of our ongoing discussion, we here mention a few of those factors as follows: maintaining the desired level of homogeneity or stratification in a laminar flow regime, controlling swirl intensity and direction for fluids with comparable effective viscosities and enabling a sufficiently reduced time to achieve the desired level of convective-based efficient mixing (Matsunaga & Nishino 2014; Cortes-Quiroz *et al.* 2017; Majhi *et al.* 2023). The non-dimensional form of species transport equation is given as

$$\frac{W}{r} \frac{\partial C}{\partial \theta} + U \frac{\partial C}{\partial z} = \frac{1}{Pe} \left[\frac{1}{r} \frac{\partial}{\partial r} \left(r \frac{\partial C}{\partial r} \right) + \frac{1}{r^2} \frac{\partial^2 C}{\partial \theta^2} + \frac{\partial^2 C}{\partial z^2} \right]. \quad (2.21)$$

In (2.21), the Péclet number $Pe (= u_{av}R/D_0)$ is defined as the ratio of the convection strength to the diffusion strength.

To obtain the mixing performance of the constituent fluids in the chosen fluidic device under the modulation of vortical flows, we solve (2.21) using our in-house developed finite volume-based code (Patankar 1980). The analytically derived flow velocity profiles (both tangential and axial velocities) are used to solve the species transport (2.21). The non-dimensional boundary conditions for the species transport (2.21) are outlined next in (2.22a–c)

$$\text{Along the radial direction: } \frac{\partial C}{\partial r} \Big|_{r=0} = 0; \quad \frac{\partial C}{\partial r} \Big|_{r=1} = 0, \quad (2.22a)$$

$$\text{Along the azimuthal direction: } C_{(\theta=0)} = C_{(\theta=2\pi)}; \quad \frac{\partial C}{\partial \theta} \Big|_{\theta=0} = \frac{\partial C}{\partial \theta} \Big|_{\theta=2\pi}, \quad (2.22b)$$

$$\text{Along the axial direction: } C_{(z=0)} = \begin{cases} 1, & 0 \leq \theta < \pi \\ 0, & \pi \leq \theta < 2\pi \end{cases}; \quad \frac{\partial C}{\partial z} \Big|_{z=L} = 0. \quad (2.22c)$$

We briefly discuss the numerical framework employed in this study to solve (2.21) using the aforementioned boundary conditions (2.22a–c) in the forthcoming section.

2.3.1. Numerical analysis

As mentioned before, we solve the species transport (2.21) numerically by employing our in-house developed finite volume code. We use a power-law scheme for the discretization of (2.21) to obtain converged solutions for a higher value of the Péclet number (Pe) using the boundary conditions given in (2.22a–c).

The mixing performance is typically assessed by analysing the variation of mixing efficiency with respect to the mixing methods (active or passive) and by varying the involved parameters such as Péclet number, characteristic length scale of the device etc., within their permissible range. In the present endeavour, to elucidate the mixing performance, we calculate mixing efficiency η_m by using the expression given below (Wang *et al.* 2015; Gaikwad, Kumar & Mondal 2020; Shyam *et al.* 2021; Kaushik *et al.* 2022)

$$\eta_m(z) = \left[1 - \left(\frac{\int_A |C_i(r, \theta, z) - C_\infty| dr d\theta}{\int_A |C_0(r, \theta) - C_\infty| dr d\theta} \right) \right] \times 100 \%. \quad (2.23)$$

In (2.23), C_∞ represents the dimensionless concentration of species at a perfectly mixed state, which is usually taken as 0.5.

As evident from (2.23), η_m gives the efficiency at each axial location of the channel. Therefore, we can estimate the mixing length from this expression, which, in turn, will allow us to predict the required size of the proposed mixing assay. We mention here that, at the channel inlet, $C_0 = 1, 0$ in the upper half and lower half, respectively, as shown in figure 1. Note that $\eta_m \in (0, 1)$ in (2.23) can take any value between zero and one. Important to mention here is that the zero value implies no mixing of the constituent components, while a value of unity indicates a completely mixed state of the participating components.

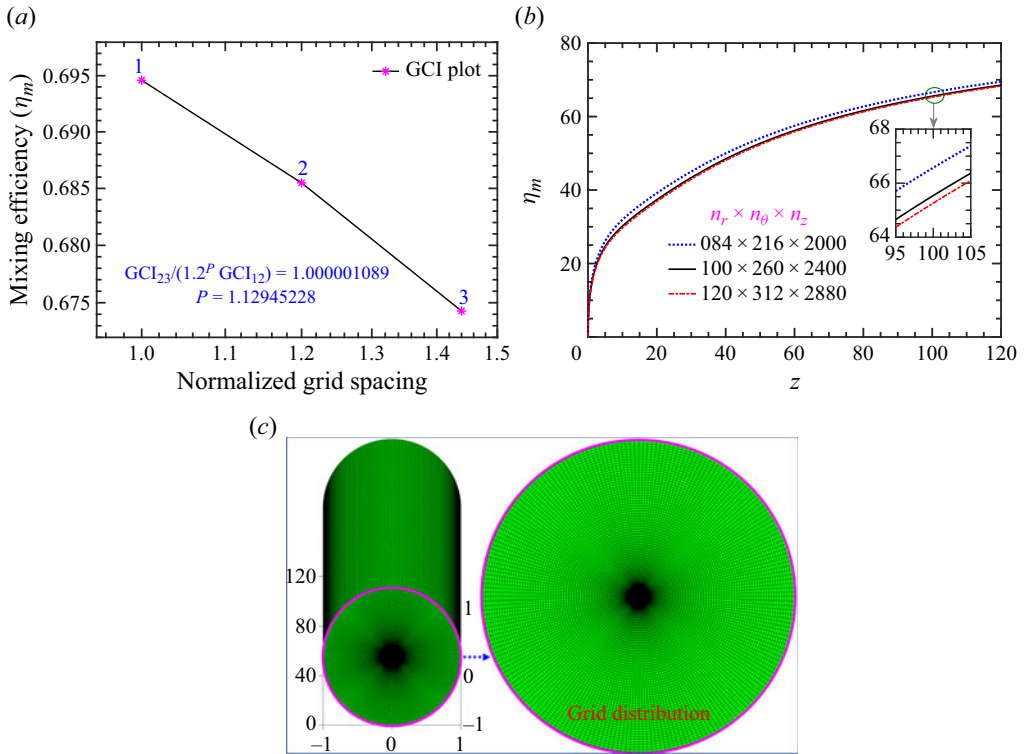


Figure 4. (a) Plot showing the GCI for three different grid refinements, defined with a dummy variable for $\Delta = 1.2^0, 1.2^1, 1.2^2$. (b) The mixing efficiency at the pipe outlet is plotted for three distinct grid refinements in all directions as considered for GCI analysis. The other parameters considered for these plots (a,b) are Reynolds number ($Re = 100$), transition radius ($r_t = 0.9$), Péclet number ($Pe = 2600$) and power-law index ($n = 0.8$). (c) Typical grid structure and distribution are shown for the fluidic configuration considered here with an axial distance of 120 times the radius ($z = 120R$).

2.3.2. Grid performance analysis

Just to ascertain that the mixing efficiency, estimated numerically in the present analysis, does not have any grid resolution bias, we perform a grid performance test for a set of other parameters as $n = 0.8$ at $Pe = 2600$, $r_t = 0.9$ and $Re = 100$, as shown in figure 4. In doing so, we calculate the grid convergence index (GCI), as shown in figure 4(a).

To conduct this analysis, we considered a grid number with a dummy variable Δ , proportional to the dimension of the chosen model, in three mutually perpendicular directions. Here, we vary Δ with a spacing ratio of 1.2 in three mutually perpendicular directions having finer grid distributions for the $\Delta = 1.2^1$ and $\Delta = 1.2^2$ cases than that of the case $\Delta = 1.2^0$. Note that a typical grid structure corresponding to $\Delta = 1.2^0$ pertaining to the chosen fluidic configuration with an axial distance of 120 times the pipe radius ($L = 120R$) is shown in figure 4(c). From the depicted results of GCI for two sets of grid refinements in figure 4(a), we find that $GCI_{23}/1.2^P GCI_{12} \approx 1$ with an order of convergence $P = 1.129$, where $GCI_{12} = 4.98\%$ and $GCI_{23} = 6.12\%$. This calculation of GCI suggests that the solutions indeed lie comfortably within the asymptotic range of convergence, affirming the reliability of the results of this endeavour.

Following this GCI plot, we show in figure 4(b) the axial variation of mixing efficiency for three distinct grid refinements in all directions, as considered for GCI analysis.

The parameters considered for this plot are $n = 0.8$, $Pe = 2600$, $r_t = 0.9$ and $Re = 100$. Remarkably, with a change in grid refinement from 62.40×10^6 to 107.83×10^6 elements, we observe an insignificant variation in the mixing efficiency, with a percentage change below 1% at a specific axial location, $z = 100$. Based on these observations from [figure 4\(a,b\)](#), we consider $\Delta = 1.2^1$, equivalently $100 \times 260 \times 2400$ ($= 62.4 \times 10^6$) grids for the subsequent analysis, as discussed in the upcoming sections.

2.3.3. Solute mixing: prediction, transition and efficiency

From the discussion above in §2.2.3, it is apparent that the shear-thinning fluids have a significant influence on the swirl velocity. Also, we understand from the foregoing discussion that, for the shear-thinning fluids ($n < 1$), convection has a dominant influence over molecular diffusion on the underlying mixing for higher values of Re , as discussed next.

The variation of mixing efficiency along the axial direction for different values of power-law index is depicted in [figure 5](#). The other parameters considered for this plot are $Pe = 2600$, $Re = 100$ and $r_t = 0.7$. We can see from [figure 5\(a\)](#) that, with a decreasing value of the power-law index, the mixing efficiency increases along the axial direction. It may be mentioned here that, for the shear-thinning fluids ($n < 1$), the effect of convection on the underlying mixing is better realized for a decreasing value of the transition radius and increasing magnitude of Re . The higher strength of rotational inertia for $Re = 100$ and more shear-thinning behaviour of the participating fluids for $n = 0.8$ lead to an increase of the tangential flow velocity at a given strength of inlet swirl. The higher tangential velocity is responsible for the augmented chaotic nature of the candidate fluids due to an increase in the contact area between them, which, in turn, promotes convective mixing along the axial direction. It is because of this reason that the mixing efficiency of shear-thinning fluids becomes higher, as witnessed in [figure 5\(a\)](#). We show, in [figure 5\(b\)](#), the influence of transition radii on the axial variation of mixing efficiency. The inference obtained from the depicted variation of the swirl velocity profile versus transition radius (see [figure 3a](#)) suggests that the swirl intensity is higher for a smaller transition radius, i.e. $r_t = 0.7$. As can be seen from [figure 5\(b\)](#), for the smaller value of r_t , the mixing efficiency at the channel outlet becomes higher, attributed primarily to a higher intensity of swirl. Notably, for a given r_t , the mixing efficiency at any axial location becomes higher for the shear-thinning fluids ($n < 1$) compared with the shear-thickening fluids ($n > 1$), as seen in [figure 5\(b\)](#). For a specified strength of inlet swirl, the rate of swirl decay is slower for shear-thinning fluids (see [figure 3d](#)), which renders better mixing efficiency for this class of fluids at any axial location.

As the prime focus of this endeavour is to investigate the mixing performance of non-Newtonian fluids/solutes, we make an attempt in [figure 6](#) to plot the variation of mixing efficiency (η_m) with flow behaviour index (n), characterizing the rheological behaviour of the inelastic non-Newtonian fluids considered in this analysis. We may mention here that the mixing transition is a consequence of the appearance and development of small-scale three-dimensional swirl structures in the flow field. The large excursions corresponding to large vortex structures typically depend on Re , and are responsible for convective-based mixing in shorter length (Breidenthal 1981). Precisely by depicting [figure 6](#), we would like to demonstrate how the transition in mixing occurs in a swirl-driven flow environment as modulated by the fluid rheology. The other parameters are $Re = 100$, $Pe = 2600$ and $r_t = 0.7$.

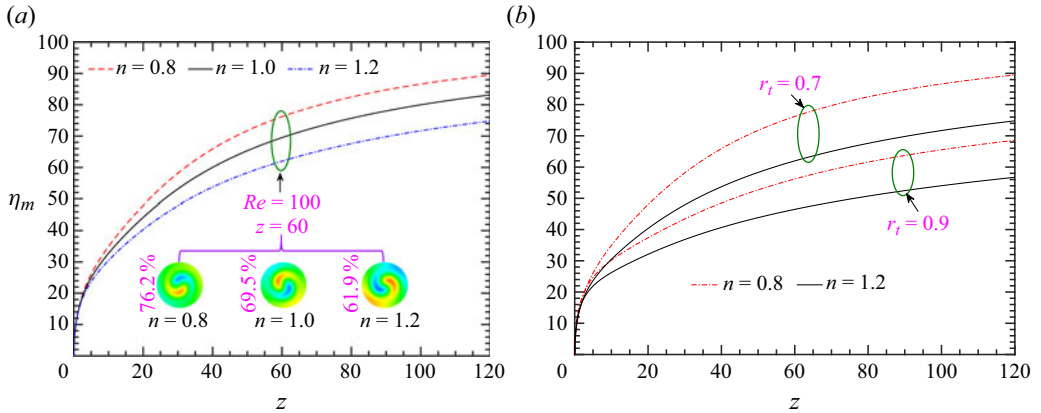


Figure 5. The plot of mixing efficiency along the axial direction: (a) with change in value of the power-law index ($n = 0.8, 1.0, 1.2$), where the other parameters considered for the plot are $Re = 100, Pe = 2600$ and $r_t = 0.7$; and (b) at two different transition radii ($r_t = 0.7, 0.9$) for shear-thinning ($n = 0.8$) and shear-thickening fluids ($n = 1.2$), where the other parameters considered for the plot are $Re = 100, Pe = 2600$.

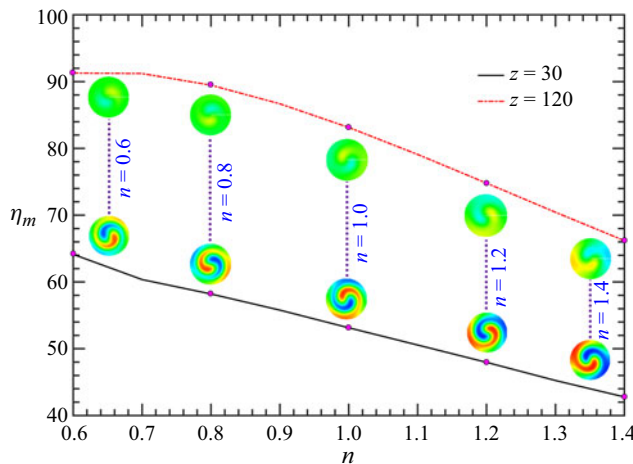


Figure 6. The plot shows qualitative aspect of mixing efficiency using concentration contour with change in the power-law index ($n = 0.6, 0.8, 1.0, 1.2$, and 1.4) at two different axial locations, $z = 30$ and 120 . The indicated concentration contours are used to show the qualitative aspect of advective mixing for a shear-thinning fluid at $n = 0.6$ compared with diffusive mixing for a shear-thickening fluid at $n = 1.4$. It is based on the complete rotation of fluid at $n = 0.6$ compared with $n = 1.4$. The other parameters considered for this analysis are $Re = 100, Pe = 2600$ and $r_t = 0.7$.

The higher internal convection of the constituent fluids, which follows a nonlinear trend with increasing n , as demonstrated by the concentration contours in figure 6, leads to better mixing being achieved in swirl-driven flow environments. It may be mentioned here that the concentration contours give a good indication of the impact of swirl on vortex formation. At an axial location $z = 30$, the concentration contour for $n = 0.6$ (see concentration contour of figure 6) exhibits a complete bulk fluid rotation compared with the reference vortex formed for $n = 1.4$ (see supplementary movies 5–7 for a clear insight). This observation indicates that convection-based mixing dominates

over molecular diffusion for $n = 0.6$. Depicted contours in [figure 6](#) suggest that, for more shear-thickening behaviour of the candidate fluids ($n = 1.4$), mixing based on molecular diffusion is clearly visible to the naked eye at an axial location of $z = 30$ compared with $z = 120$. As can be verified from [figure 6](#), with increase of the shear-thinning nature of the constituent components, the underlying mixing is seen to become more pronounced regardless of the magnitude of Re , transition radius and Pe . A lesser apparent viscosity of constituent fluids having a more shear-thinning nature for a given deformation rate (here, strength of inlet swirl) inhibits faster attenuation of swirl for its given strength, which, in turn, ensures better mixing performance at any axial location, as witnessed in [figure 6](#).

It may be mentioned here that the transmission of a given strength of the inlet swirl through the participating fluids largely relies on the momentum transport, which, in turn, depends on the Reynolds number. Thus, in a swirl-driven flow environment, underlying mixing of constituent fluids will be governed by both the inevitable molecular diffusion and chaotic advection. Considering this aspect, we plot in [figure 7\(a\)](#) the variation of mixing efficiency with Re for three different values of n ($= 0.8, 1.0$ and 1.2). The following parameters are considered for this plot as $Pe = 2600, z = 100$ and $r_t = 0.7$. We discuss two important observations as follows. First, the mixing efficiency is seen to be higher for shear-thinning fluids ($n < 1$) compared with shear-thickening fluids ($n > 1$). We attribute this observation to the lesser apparent viscosity of shear-thinning fluids, which prevents faster swirl decay. Second, a higher inertial effect for higher Reynolds number accelerates the swirl motion penetrating much deeper into the channel before attenuation. However, at lower Re , impeding viscous resistance leads to swirl decay over shorter distances from the inlet. This observation is justifiable qualitatively from the mixing concentration contours depicted in [figure 7\(b\)](#). It is because of the diminishing effect of inlet swirl at low Re that we observe a linear trend of mixing in regime-I of [figure 7\(a\)](#), attributed primarily to the diffusion-based mixing. The contours depicted in [figure 7\(b\)](#) suggest that, for the smaller values of Re ($= 1, 10$), the effect of inlet swirl is not translated into the downstream locations of the fluidic configuration. This observation is attributed to the weaker rotational fluid motion developed at the pipe inlet for smaller values of Re . It is because of this reason that we obtain diffusion-based mixing for smaller Re even at a further downstream location of the pipe, as witnessed in [figure 7](#). The role of convection-based mixing is shown in regime-II, which follows the nonlinear trend. For Re greater than 10, bulk fluids rotate more than 90° . This flow structure helps to increase the contact surface area between the fluid layers and enhances convection-based mixing, as supported by the contours shown in [figure 7\(b\)](#).

The contours illustrating the mixing efficiency in [figures 6](#) and [7](#) establish the dependency of the underlying mixing on the power-law index ($n \in 0.6-1.4$) and Reynolds number ($Re \in 10^0-10^2$). The discussion made above in the context of [figures 6](#) and [7](#) underscores that convection-dominated mixing becomes prominent for shear-thinning fluids with higher Re . To substantiate this observation, we next make an effort to establish a correlation among the mixing efficiency (η_m), power-law index and Reynolds number. The developed correlation, represented by a second-order polynomial, exhibits a high degree of fit with a coefficient of determination value of 0.9935. The developed explicit, quadratic form of η_m in terms of the independent variables, i.e. power-law index and Reynolds number at the pipe outlet ($z = 120$) can be expressed as follows:

$$\eta_m = a_1 + a_2n + a_3Re - a_4n^2 - a_5nRe + a_6Re^2. \quad (2.24)$$

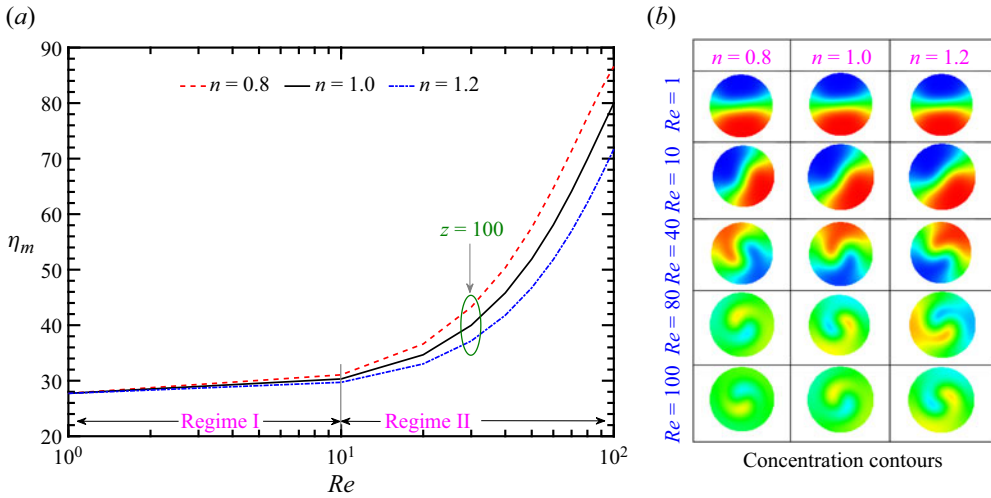


Figure 7. (a) The plot shows mixing efficiency (left side) as a function of Reynolds number (1 to 100), as well as shear thinning and thickening ($n = 0.8$ and 1.2 , respectively), in addition to Newtonian fluid ($n = 1.0$) at an axial location, $z = 100$. (b) The qualitative aspect of mixing efficiency (right side) using concentration contours with change in the same n at $Re = 1, 10, 40, 80$ and 100 is shown. On increasing the Reynolds number, advective mixing (regime II) is obtained at $Re = 100$ compared with diffusive (regime I) at $Re = 1$ and 10 based on complete rotation of fluid compared with only twist, respectively. The other parameters considered for this analysis are $Pe = 2600$ and $r_t = 0.7$.

Here, the constants a_1, a_2, a_3, a_4, a_5 and a_6 are 23.31, 15.92, 0.8756, 10.9, 0.3503 and 0.0002416, respectively. Note that the proposed correlation in (2.24) corresponds to the data set obtained for $r_t = 0.7$ and $Pe = 2600$.

On using (2.24), we obtain the following insights, as discussed next. The mixing efficiency at the channel outlet ($z = 120$) becomes higher with increasing magnitude of Re and for an enhanced shear-thinning nature of the fluid. This inference effectively supports the findings depicted in figures 6 and 7. Hence, it becomes evident that the convective-based mixing efficiency is significantly influenced by both the rheology of the constituent fluids and the flow Reynolds number.

3. Summary, perspective and outlook

In the present analysis, we investigate the effect of swirl flow (vortical flow) on the mixing of non-Newtonian fluids in a narrow cylindrical pipe under laminar flow conditions. We analytically derive the expression for the swirl velocity profile by superimposing the fully developed flow and applying the Rankine vortex condition at the channel inlet. We incorporate analytically obtained flow velocities (both swirl (tangential) and axial velocities) into the species transport equation to obtain the concentration distribution of the constituent fluids/solutes along the cross-section of the chosen fluidic configuration. We examine the influence of inlet swirl by varying pertinent parameters such as flow behaviour (power-law) index ($n = 0.6-1.4$), Reynolds number ($Re = 10^0-10^2$) and transition radius ($r_t = 0.7-0.9$).

Our findings reveal that an increase in the value of the power-law index, signifying the change in behaviour of the constituent fluids from shear thinning to shear thickening, results in an increase in the fluids' apparent viscosity for a given inlet swirl. We observe that the decay of swirl is critically dependent on the magnitude of the power-law index

or flow behaviour index. We unveil through this analysis that both the power-law index and the Reynolds number significantly impact the length of swirl decay. This increased apparent viscosity of the constituent fluids with higher values of power-law index leads to a reduction in the magnitude of both axial and tangential velocities. It is demonstrated that decreasing the value of the transition radius and increasing the magnitude of the Reynolds number leads to an enhancement of swirl intensity to act over a greater extent of the flow configuration, attributed primarily to the combined effects of a higher value of the radial pressure gradient and a reduced wall shear stress. Based on the findings obtained from our simulations, we elucidate how swirl alters the flow structure, inducing rotation and enhancing the contact surface area of the participating fluids. Our study demonstrates that chaotic convection, or the swirl-driven rotation of the fluid, plays a significant role in enhancing mixing efficiency at a higher Reynolds number. We believe that the insights gained from this study may strengthen the fundamental idea of vortex-assisted mixing for non-Newtonian fluids in a narrow fluidic confinement. The current work may be particularly valuable for researchers aiming to enhance transport capabilities and convective mixing through the use of swirl flow, especially by altering the rheological properties of base fluids, like water through a polymer dilution, to change their rheological behaviour.

Supplementary movies. Supplementary movies are available at <https://doi.org/10.1017/jfm.2024.792>.

Acknowledgements. D.K. gratefully acknowledges funding from the Prime Minister Research Fellowship (PMRF), Ministry of Education, Govt. of India to carry out this research work. The authors sincerely thank the anonymous reviewers for their insightful comments to improve the quality of the manuscript.

Declaration of interests. The authors report no conflict of interest.

Author ORCIDs.

 Dhananjay Kumar <https://orcid.org/0000-0001-8988-4890>;

 Pranab Kumar Mondal <https://orcid.org/0000-0002-9368-1532>.

Author contributions. D.K.: formal analysis, data curation, conceptualization, investigation, methodology, software, visualization, validation, writing – original draft. P.K.M.: conceptualization, funding acquisition, methodology, project administration, resources, supervision, validation, writing – review, and editing.

REFERENCES

- ABRAMOWITZ, M. & STEGUN, I.A. 1970 *Handbook of Mathematical Functions: With Formulas, Graphs, and Mathematical Tables*. National Bureau of Standards.
- AFZAL, A. & KIM, K.-Y. 2014 Flow and mixing analysis of non-Newtonian fluids in straight and serpentine microchannels. *Chem. Engng Sci.* **116**, 263–274.
- ALEKSEENKO, S.V., KUIBIN, P.A., OKULOV, V.L. & SHTORK, S.I. 1999 Helical vortices in swirl flow. *J. Fluid Mech.* **382**, 195–243.
- BINAGIA, J.P., PHOA, A., HOUSIADAS, K.D. & SHAQFEH, E.S.G. 2020 Swimming with swirl in a viscoelastic fluid. *J. Fluid Mech.* **900**, A4.
- BIRD, R.B., STEWART, W.E. & LIGHTFOOT, E.N. 2006 *Transport Phenomena*, 2nd edn. John Wiley & Sons, Inc.
- BREIDENTHAL, R. 1981 Structure in turbulent mixing layers and wakes using a chemical reaction. *J. Fluid Mech.* **109**, 1–24.
- CETEGEN, B.M. & MOHAMAD, N. 1993 Experiments on liquid mixing and reaction in a vortex. *J. Fluid Mech.* **249**, 391–414.
- CHEN, Y., LV, Z., WEI, Y. & LI, J. 2022 Mixing performance of the induced charge electro-osmosis micromixer with conductive chamber edges for viscoelastic fluid. *Phys. Fluids* **34**, 083110.
- CORTES-QUIROZ, C.A., AZARBADEGAN, A. & ZANGENEH, M. 2017 Effect of channel aspect ratio of 3-D T-mixer on flow patterns and convective mixing for a wide range of Reynolds number. *Sensors Actuators B* **239**, 1153–1176.

- COSENTINO, A., MADADI, H., VERGARA, P., VECCHIONE, R., CAUSA, F. & NETTI, P.A. 2015 An efficient planar accordion-shaped micromixer: from biochemical mixing to biological application. *Sci. Rep.* **5**, 17876.
- DAS, S., BANIK, M., CHEN, G., SINHA, S. & MUKHERJEE, R. 2015 Polyelectrolyte brushes: theory, modelling, synthesis and applications. *Soft Matter* **11**, 8550–8583.
- DEEN, W.M. 2016 *Introduction to Chemical Engineering Fluid Mechanics*. Cambridge University Press.
- DJENIDI, L. & MOGHADERI, B. 2006 Numerical investigation of laminar mixing in a coaxial microreactor. *J. Fluid Mech.* **568**, 223–242.
- GAIKWAD, H.S., KUMAR, G. & MONDAL, P.K. 2020 Efficient electroosmotic mixing in a narrow-fluidic channel: the role of a patterned soft layer. *Soft Matter* **16**, 6304–6316.
- GAIKWAD, H.S., MONDAL, P.K. & WONGWISES, S. 2018 Softness induced enhancement in net throughput of non-linear bio-fluids in nanofluidic channel under EDL phenomenon. *Sci. Rep.* **8**, 7893.
- GRASSIA, P. 2020 Viscous and electro-osmotic effects upon motion of an oil droplet through a capillary. *J. Fluid Mech.* **899**, A31.
- HADIGOL, M., NOSRATI, R., NOURBAKHS, A. & RAISEE, M. 2011 Numerical study of electroosmotic micromixing of non-Newtonian fluids. *J. Non-Newtonian Fluid Mech.* **166**, 965–971.
- HENDERSON, G.A. & ALDRIDGE, K.D. 1992 A finite-element method for inertial waves in a frustum. *J. Fluid Mech.* **234** (1), 317.
- HERREMAN, W., NORE, C., CAPPANERA, L. & GUERMOND, J.L. 2021 Efficient mixing by swirling electrovortex flows in liquid metal batteries. *J. Fluid Mech.* **915**, A17.
- HUANG, Y., CHEN, J., WONG, T. & LIOW, J.L. 2016 Experimental and theoretical investigations of non-Newtonian electro-osmotic driven flow in rectangular microchannels. *Soft Matter* **12**, 6206–6213.
- INGHAM, D.B., KEEN, D.J., HEGGS, P.J. & MORTON, B.R. 1990 Recirculating pipe flows. *J. Fluid Mech.* **213** (1), 443.
- KAPLAN, W. 1981 *Advanced Mathematics for Engineers*. Addison Wesley Higher Education.
- KATHAIL, A., PRANAV, C.M. & KAUSHIK, P. 2019 Inlet swirl decay of non-Newtonian fluid in laminar flows through tubes. *Sadhana* **44**, 238.
- KAUSHIK, P., SHYAM, S. & MONDAL, P.K. 2022 Mixing in small scale fluidic systems swayed by rotationality effects. *Phys. Fluids* **34**, 062008.
- KIM, T.Y. 2024 Analytical solution for laminar entrance flow in circular pipes. *J. Fluid Mech.* **979**, A51.
- KITOH, O. 1991 Experimental study of turbulent swirling flow in a straight pipe. *J. Fluid Mech.* **225**, 445–479.
- KIYA, M., FUKUSAKO, S. & ARIF, M. 1971 Laminar swirling flow in the entrance region of a circular pipe. *Bulletin of JSME* **14** (73), 659–670.
- KREITH, F. & SONJU, O.K. 1965 The decay of a turbulent swirl in a pipe. *J. Fluid Mech.* **22** (2), 257–271.
- KRISHNAVENI, T., RENGANATHAN, T., PICARDO, J.R. & PUSHAVANAM, S. 2017 Numerical study of enhanced mixing in pressure-driven flows in microchannels using a spatially periodic electric field. *Phys. Rev. E* **96** (3), 033117.
- KUMAR, D., GAIKWAD, H.S., KAUSHIK, P. & MONDAL, P.K. 2023 Swirl driven solute mixing in narrow cylindrical channel. *Phys. Fluids* **35** (6), 063604.
- KUMAR, D., SHAKYA, S.M.K. & KAUSHIK, P. 2020 Inlet swirl decay and mixing in a laminar micro-pipe flow with wall slip. *Phys. Fluids* **32** (2), 022008.
- LAY, J.E. 1959 An experimental and analytical study of vortex-flow temperature separation by superposition of spiral and axial flow. Part 2. *J. Heat Transfer* **81** (3), 213–221.
- MADANA, V.S.T. & ASHRAF ALI, B. 2020 Numerical investigation of engulfment flow at low Reynolds numbers in a T-shaped microchannel. *Phys. Fluids* **32** (7), 072005.
- MADDAHIAN, R., KEBRIAE, A., FARHANIEH, B. & FIROOZABADI, B. 2011 Analytical investigation of boundary layer growth and swirl intensity decay rate in a pipe. *Arch. Appl. Mech.* **81** (4), 489–501.
- MAJHI, M., NAYAK, A.K. & WEIGAND, B. 2023 Electroosmotic mixing of non-Newtonian fluid in an optimized geometry connected with a modulated microchamber. *Phys. Fluids* **35** (3), 032013.
- MATSUNAGA, T. & NISHINO, K. 2014 Swirl-inducing inlet for passive micromixers. *RSC Adv.* **4** (2), 824–829.
- MEHTA, S.K., PATI, S. & MONDAL, P.K. 2021 Numerical study of the vortex-induced electroosmotic mixing of non-Newtonian biofluids in a nonuniformly charged wavy microchannel: effect of finite ion size. *Electrophoresis* **42** (23), 2498–2510.
- MORTON, B.R. 1969 The strength of vortex and swirling core flows. *J. Fluid Mech.* **38** (2), 315–333.
- NWANI, B.N., MERHABEN, C., GATES, I.D. & BENNEKER, A.M. 2022 Numerical simulation of electrokinetic control of miscible viscous fingering. *Phys. Fluids* **34** (12), 124104.
- PARCHEN, R.R. & STEENBERGEN, W. 1998 An experimental and numerical study of turbulent swirling pipe flows. *J. Fluids Engng* **120** (1), 54–61.
- PATANKAR, S.V. 1980 *Numerical Heat Transfer and Fluid Flow*. CRC Press.
- READER-HARRIS, M.J. 1994 The decay of swirl in a pipe. *Intl J. Heat Fluid Flow* **15** (3), 212–217.

Mixing of inelastic non-Newtonian fluids with inlet swirl

- REZK, A.R., QI, A., FRIEND, J.R., LI, W.H. & YEO, L. Y. 2012 Uniform mixing in paper-based microfluidic systems using surface acoustic waves. *Lab on a Chip* **12** (4), 773–779.
- ROUQUIER, A., POTHÉRAT, A. & PRINGLE, C.C.T. 2019 An instability mechanism for particulate pipe flow. *J. Fluid Mech.* **870**, 247–265.
- SARMA, R., GAIKWAD, H. & MONDAL, P.K. 2017 Effect of conjugate heat transfer on entropy generation in slip-driven microflow of power law fluids. *Nanoscale Microscale Thermophys. Engng* **21** (1), 26–44.
- SHYAM, S., MONDAL, P.K. & MEHTA, B. 2021 Magneto-fluidic mixing of a ferrofluid droplet under the influence of a time-dependent external field. *J. Fluid Mech.* **917**, A15.
- SIBULKIN, M. 1962 Unsteady, viscous, circular flow. Part 3. Application to the Ranque-Hilsch vortex tube. *J. Fluid Mech.* **12** (02), 269–293.
- STEENBERGEN, W. & VOSKAMP, J. 1998 The rate of decay of swirl in turbulent pipe flow. *Flow Meas. Instrum.* **9** (2), 67–78.
- STOKES, J.R., GRAHAM, L.J.W., LAWSON, N.J. & BOGER, D.V. 2001a Swirling flow of viscoelastic fluids. Part 1. Interaction between inertia and elasticity. *J. Fluid Mech.* **429**, 67–115.
- STOKES, J.R., GRAHAM, L.J.W., LAWSON, N.J. & BOGER, D.V. 2001b Swirling flow of viscoelastic fluids. Part 2. Elastic effects. *J. Fluid Mech.* **429**, 117–153.
- STONE, H.A., STROOCK, A.D. & AJDARI, A. 2004 Engineering flows in small devices: microfluidics toward a lab-on-a-chip. *Annu. Rev. Fluid Mech.* **36**, 381–411.
- TALBOT, L. 1954 Laminar swirling pipe flow. *J. Appl. Mech.* **21** (1), 1–7.
- TAYLOR, G.I. 1950 The boundary layer in the converging nozzle of a swirl atomizer. *Q. J. Mech. Appl. Maths* **3** (2), 129–139.
- TUMIN, A. 1996 Receptivity of pipe Poiseuille flow. *J. Fluid Mech.* **315**, 119–137.
- VAGNER, S.A. & PATLAZHAN, S.A. 2019 Flow structure and mixing efficiency of viscous fluids in microchannel with a striped superhydrophobic wall. *Langmuir* **35** (49), 16388–16399.
- VERPOORTE, E. & DE ROOIJ, N.F. 2003 Microfluidics meets MEMS. *Proc. IEEE* **91** (6), 930–953.
- WANG, J., WANG, J., FENG, L. & LIN, T. 2015 Fluid mixing in droplet-based microfluidics with a serpentine microchannel. *RSC Adv.* **5** (126), 104138–104144.
- WHITTAKER, E.T. 1903 An expression of certain known functions as generalized hypergeometric functions. *Bulletin of the American Mathematical Society* **10** (3), 125–134.
- YAO, S. & FANG, T. 2012 Analytical solutions of laminar swirl decay in a straight pipe. *Commun. Nonlinear Sci. Numer. Simul.* **17** (8), 3235–3246.